

Ciprofloxacin Electrochemical Sensor Using Copper–Iron Mixed Metal Oxides Nanoparticles/Reduced Graphene Oxide Composite

Jedsada Chuiprasert, Sira Srinives,* Narin Boontanon, Chongrak Polprasert, Nudjarin Ramungul, Apisit Karawek, and Suwana Kitpati Boontanon*



Cite This: *ACS Omega* 2024, 9, 23172–23183



Read Online

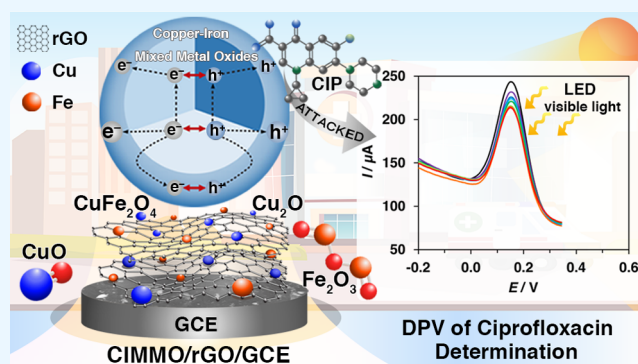
ACCESS |

Metrics & More

Article Recommendations

Supporting Information

ABSTRACT: The harmful effects of antibiotic proliferation on the environment and its persistent nature are urgent global problems. Ciprofloxacin (CIP) is a fluoroquinolone-class antibiotic agent used widely to treat pathogen-related diseases in humans and animals. Its excretion into surface water causes antibiotic resistance in microbes, resulting in difficult-to-treat or untreatable infectious diseases. This study developed a simple and efficient electrochemical sensor to detect CIP. Hydrothermal chemistry was utilized to synthesize an electrophotocatalytic composite of copper–iron mixed metal oxides (CIMMO) on reduced graphene oxide (rGO) (CIMMO/rGO). The composite was employed in an electrochemical sensor and exhibited outstanding performance in detecting CIP. The sensor was operated in differential pulse voltammetry (DPV) mode under light source illumination. The sensor yielded a linear response in the concentration range of 0.75×10^{-9} – 1.0×10^{-7} mol L⁻¹ CIP and showed a limit of detection (LOD) of 4.74×10^{-10} mol L⁻¹. The excellent sensing performance of the composite is attributable to the synergic effects between CIMMO nanoparticles and rGO, which facilitate photoinduced electron–hole separation and assist in the indirect electrochemical reactions/interactions with CIP.



1. INTRODUCTION

Antibiotic resistance (ABR) is a global issue related to the overuse and misuse of antibiotics, drugs that treat bacterial infections. Such inappropriate use of antibiotics results in their contamination in surface water and groundwater and the potential development of superpathogens with ABR.¹ Ciprofloxacin (CIP, C₁₇H₁₈FN₃O₃), a synthetic, second-generation, fluoroquinolone-class antibiotic, has been used to treat Gram-negative and Gram-positive infections in humans and animals.² Overuses of CIP have led to pollution and contamination of excessive and unmetabolized CIP in water sources, contributing to the ABR issue. CIP was detected at ng L⁻¹ to mg L⁻¹ levels in surface, ground, and drinking water as reported in recent studies.^{3,4} Conventional techniques, including capillary electrophoresis, gas chromatography (GC), and high-performance liquid chromatography with tandem mass spectrometry (HPLC–MS/MS) are currently used as standard methods for the detection of CIP.⁵ Although the detection results from these conventional techniques are precise and reliable, they rely heavily on costly equipment and complex procedures. Thus, there is a need for an easy-to-use, mobile, sensitive, and selective device for CIP detection in water.

Electrochemical sensors are a group of low-cost, lightweight, and mobile devices that can serve as an ideal platform for the detection of antibiotics.^{6–9} The devices utilize electrochemical

reactions and interactions between a target chemical and a sensitive element to generate the sensing signal.¹⁰ Bagheri et al. synthesized an electrochemical sensor using magnetic multi-walled carbon nanotubes (MMWCNTs) and a molecularly imprinted polymer (MIP) as a sensitive element for CIP detection. They reported a limit of detection (LOD) of 1.7×10^{-9} mol L⁻¹.¹¹ Li et al. used an MIP of gold nanoparticle/black phosphorus nanocomposites for selective detection of pefloxacin. The composites demonstrated a broad linear detection range with an LOD of 0.80×10^{-9} mol L⁻¹.¹² Our group reported the production of an electrochemical sensor utilizing an MIP composite of polyaniline, poly(*o*-phenylenediamine), and reduced graphene oxide (rGO) as the sensitive element. The sensor realized an LOD of 5.28×10^{-11} mol L⁻¹ for CIP detection with adequate reusability.¹³

Metals and metal oxides are outstanding candidates for sensitive elements because of their stability, ease of processing, and well-explored characteristics.¹⁴ Many metals, metal oxides,

Received: September 5, 2023

Revised: January 30, 2024

Accepted: March 21, 2024

Published: May 21, 2024



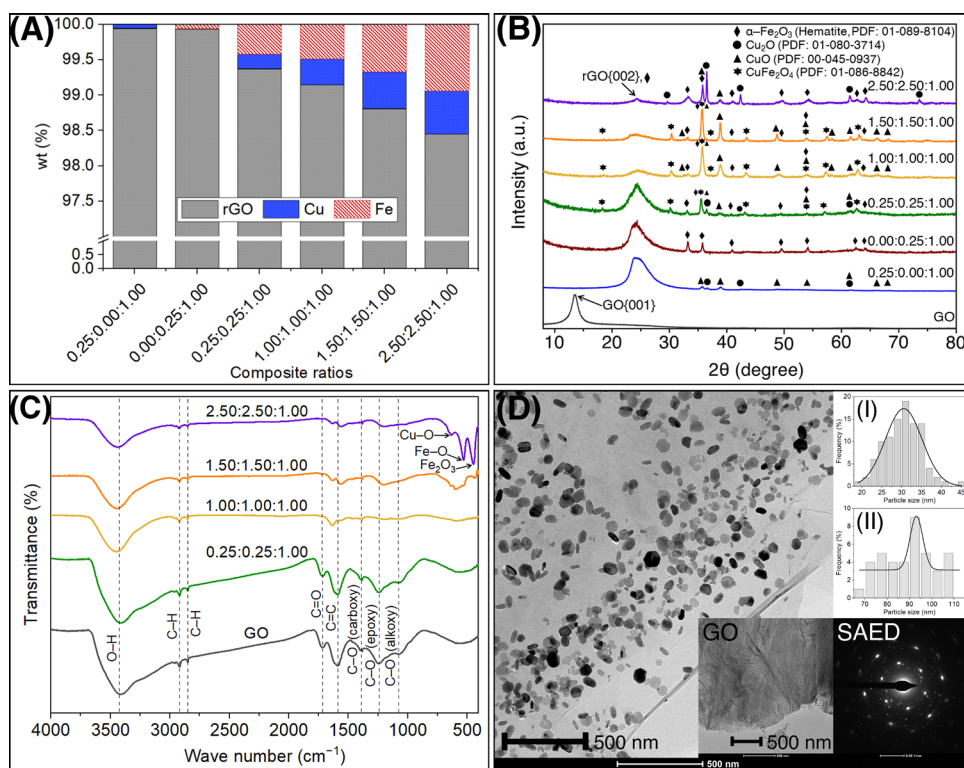


Figure 1. Analytical results from the composite samples: XRF analysis (A); XRD patterns (B); FT-IR spectra (C); TEM of 0.25:0.25:1.00 CIMMO/rGO (D), GO (D, Inset), average size distributions of CIMMO nanoparticles with a Gaussian-fitting curve (D, I inset) and (D, II inset), and SAED pattern (D, Inset).

and mixed metal oxide composites, such as bismuth oxychloride,¹⁵ cobalt ferrite,¹⁶ copper–titanium dioxide (TiO_2),¹⁷ and TiO_2 –graphene,¹⁸ have been demonstrated for their electroactivity. Copper–iron mixed metal oxides (CIMMO) are combinations of iron and copper oxides with enhanced photoactivity and redox capabilities.¹⁹ Gholivand et al. synthesized a copper–iron oxides/ TiO_2 composite and used it as part of an electrochemical sensor for metformin detection in pharmaceutical products and human urine.²⁰ Iron oxides/ TiO_2 was described as the main sensitive element for the sensor, whereas the copper oxides served as a dopant that promoted metformin adsorption and charge transfer. The working group of Khalilzadeh modified a carbon screen-printed electrode with an iron (II, III) oxides (Fe_3O_4)/cellulose nanocrystals/copper nanocomposite.²¹ The electrode was sensitive to venlafaxine while operated in differential pulse voltammetry (DPV) mode.

Graphene oxide (GO), a two-dimensional (2D) carbon nanostructure, is a layered carbon sheet with structural defects from functional groups such as carboxyl, hydroxyl, and epoxy. GO can be reduced based on chemical or thermal reduction to rGO, in which a portion of the functional groups is removed. rGO provides the electrical properties of a semiconductor and is a good sensitive element or charge-transfer promotor in a sensor device.^{22,23} GO can be composited with metals and metal oxides and becomes a mixed metal oxides/rGO composite. Side reactions involve the conversion of GO to rGO due to reduction reactions occurring during chemical and thermal treatment. The mixed metal oxides can be deposited as nanoparticles on the structural defects of rGO, immobilized, and separated from one another with high surface reactivity for reactions.^{24–26} In addition, mixed metal oxides/rGO interfaces

assist in stabilizing active radicals and intermediates and promoting electron–hole separation, which enhances the catalytic activities of composites.

In this research, we synthesized the CIMMO/rGO composite following a one-step hydrothermal technique for use as a sensitive element in an electrochemical sensor. The sensor was operated in the DPV mode to detect CIP in water solutions. The solutions were prepared by using ultrapure water (UPW) or surface water. The reusability, reproducibility, and stability of the sensor were also examined to assess its practical usability.

2. RESULTS AND DISCUSSION

2.1. Physical and Chemical Characterizations.

2.1.1. Micro X-ray Fluorescence (μXRF) Analysis. The mass compositions of the composite samples were analyzed by using μXRF . The carbon element (C) from rGO was interpreted from residual data using the fundamental parameter method (Figure 1A). The 0.25:0.00:1.00 CIMMO/rGO composite sample was obtained from 2.5 mg of copper nitrate trihydrate ($\text{Cu}(\text{NO}_3)_2 \cdot 3\text{H}_2\text{O}$) and 1.0 mg of GO with no ferric chloride (FeCl_3). The composite displayed 0.06%w/w copper element (Cu) incorporated with rGO (99.04%w/w), with no iron element (Fe). The 0.00:0.25:1.00 CIMMO/rGO sample was synthesized using 2.5 mg of FeCl_3 with 1.0 mg of GO (0.00:0.25:1.00 Cu:Fe:GO). The composite exhibited 0.06% w/w Fe on 99.04%w/w rGO. Analysis of the 0.25:0.25:1.00 CIMMO/rGO revealed 0.21, 0.42, and 99.37%w/w for Cu, Fe, and rGO, respectively. Increasing the proportions of the metal precursors to 1.00:1.00:1.00 and 1.50:1.50:1.00 (1.00:1.00:1.00 and 1.50:1.50:1.00 CIMMO/rGO) produced composites with 0.37%w/w Cu, 0.48%w/w Fe, and 99.15%w/w

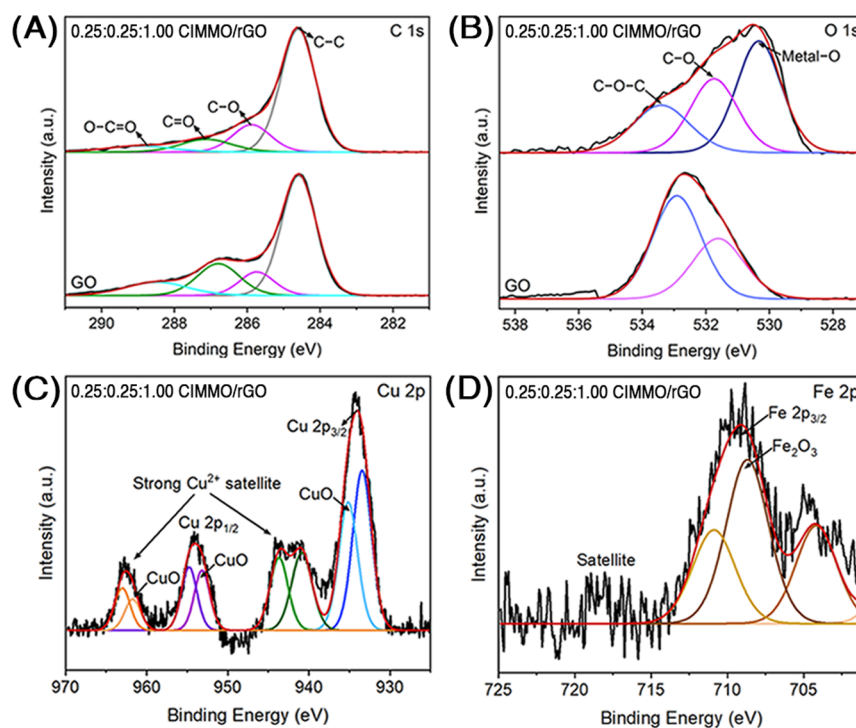


Figure 2. XPS narrow scan of GO and 0.25:0.25:1.00 CIMMO/rGO composite, focusing on C 1s (A), O 1s (B), Cu 2p (C), and Fe 2p (D).

w rGO and 0.52%w/w Cu, 0.67%w/w Fe, and 98.81%w/w rGO, respectively. Analysis of the 2.50:2.50:1.00 CIMMO/rGO provided mass compositions of 0.61, 0.94, and 98.45%w/w for Cu, Fe, and rGO, respectively.

2.1.2. X-ray Diffraction (XRD) Analysis. The crystal structures of the composites prepared from different ratios of CIMMO precursors were analyzed by XRD (Figure 1B). GO showed a single diffraction peak at 13.5° , which can be ascribed to the $\{001\}$ plane of GO structures.²⁷ All composite samples revealed a peak at 24.4° , which correlated to the $\{002\}$ plane of the rGO. The result confirmed the side reaction that converted GO to rGO during hydrothermal. The 0.25:0.00:1.00 CIMMO/rGO composite presented crystalline phases of cupric oxide (CuO) and cuprous oxide (Cu₂O). The peak positions at 35.7° , 38.9° , 48.9° , 53.9° , 61.6° , 66.3° , and 68.1° corresponded to the $\{001\}$, $\{111\}$, $\{-202\}$, $\{020\}$, $\{-113\}$, $\{-311\}$, and $\{-220\}$ crystal planes of CuO (PDF: 00-045-0937). The other three characteristic peaks at 36.7° , 42.6° , and 61.6° were attributed to the $\{111\}$, $\{200\}$, and $\{220\}$ crystal planes of Cu₂O (PDF: 01-080-3714), respectively. The diffraction pattern for 0.00:0.25:1.00 CIMMO/rGO showed peaks at 33.2° , 35.7° , 40.9° , 49.6° , 54.2° , 62.4° , and 64.2° , which correlated to the $\{104\}$, $\{110\}$, $\{113\}$, $\{024\}$, $\{116\}$, $\{214\}$, and $\{300\}$ crystal planes of the hematite iron oxide (α -Fe₂O₃) phases (octahedral and rhombohedral) (PDF: 01-089-8104), respectively. The 0.25:0.25:1.00, 1.00:1.00:1.00, and 1.50:1.50:1.00 CIMMO/rGO compositions provided similar diffraction patterns, showing signals for three crystalline phases: copper ferrite (CuFe₂O₄), α -Fe₂O₃, and CuO. Additional peaks from 0.25:0.25:1.00 and 2.50:2.50:1.00 CIMMO/rGO were observed at 36.7° , 42.6° , and 61.6° , which represented the $\{111\}$, $\{200\}$, and $\{220\}$ planes of Cu₂O, respectively. The peaks at 18.2° , 30.3° , 35.8° , 38.7° , 43.3° , 54.1° , 57.3° , and 63.2° corresponded to the $\{111\}$, $\{220\}$, $\{311\}$, $\{222\}$, $\{400\}$, $\{422\}$, $\{511\}$, and $\{440\}$ planes of CuFe₂O₄ (PDF: 01-086-8842).

2.1.3. Fourier Transform Infrared Spectroscopy (FT-IR) Analysis. FT-IR was used to analyze the chemical functionality (Figure 1C). The GO spectra peaked at 3421 cm^{-1} , indicating the presence of O–H stretching group and adsorbed water molecules. The peaks at 2915 and 2850 cm^{-1} correspond to alkyl C–H stretching. The IR transmittance peaks at 1720 , 1590 , 1390 , 1240 , and 1080 cm^{-1} correlated to the C=O stretching of carbonyl, C=C stretching, C–O stretching of carboxyl, C–O stretching of epoxy, and C–O stretching of alkoxy.^{28,29} Some GO IR transmittance peaks, revealing O–H stretching, C–H stretching, C=C stretching, and C–O stretching, were observed on the composites spectra. The O–H stretching signal at 3421 shifted to 3428 cm^{-1} , suggesting interactions between copper and iron mixed metal oxides and –OH groups.³⁰ The IR spectrum of 0.25:0.25:1.00 CIMMO/rGO appeared to be identical to the GO spectrum but with reduced peak intensity. The results demonstrated good CIMMO adhesion onto rGO and partial removal of the chemical functionalities. For 1.00:1.00:1.00, 1.50:1.50:1.00, and 2.50:2.50:1.00 CIMMO/rGO, IR transmittance peak intensities were further reduced. An additional peak appeared at 633 cm^{-1} and was interpreted as Cu–O from CuO/Cu₂O species.³¹ The 2.50:2.50:1.00 CIMMO/rGO showed two additional characteristic peaks at 533 and 447 cm^{-1} , which corresponded to Fe–O stretching from the Fe₂O₃.³² As the amount of rGO in the CIMMO/rGO composite increased, the intensity of the Cu–O and Fe–O stretching bands decreased. Therefore, it was clear that the CIMMO nanoparticles were attached and altered the IR transmittance peaks of rGO.

2.1.4. Morphology and Size Distribution Analysis. Transmission electron microscopy (TEM) images revealed the morphology of the CIMMO nanoparticles on the rGO sheet (Figure 1D). GO (Figure 1D, Inset) displayed a sheet-like structure with wrinkles and micrometer-scale dimensions. In 0.25:0.25:1.00 CIMMO/rGO, the CIMMO nanoparticles were dispersed homogeneously on the rGO sheet, showing two

average size distribution histograms with a Gaussian-fitting curve of 30.51 ± 9.22 nm (Figure 1D, I inset) and 93.12 ± 5.73 nm (Figure 1D, II inset), respectively. The selected area electron diffraction (SAED) provided clear ring patterns (Figure 1D, inset), indicating polycrystal morphologies with large grain sizes for the nanoparticles. We located four types of nanostructures in the TEM images: CuO/Cu₂O nanorods, α -Fe₂O₃ octadecahedra, α -Fe₂O₃ rhombohedra, and CuFe₂O₄ irregular nanoparticles. The CuO/Cu₂O nanorods had a width and length of 30.51 ± 9.22 and 62.73 ± 8.11 nm, respectively (Figure S1A,B). The α -Fe₂O₃ appeared as crystalline nanoparticles with octadecahedral structures³³ and a size of 85.46 ± 28.34 nm (Figure S1C). The α -Fe₂O₃ rhombohedral³⁴ nanostructure exhibited a width of 86.07 ± 28.39 nm (Figure S1D) and a length of 93.12 ± 5.73 nm (Figure S1E). The CuFe₂O₄ nanoparticles had an irregular shape³⁵ with an average width of 52.10 ± 20.03 nm (Figure S1F) and a length of 86.92 ± 18.58 nm (Figure S1G).

2.1.5. X-ray Photoelectron Spectroscopy (XPS) Analysis. XPS was utilized for the chemical composition analysis of GO and 0.25:0.25:1.00 CIMMO/rGO composite. For GO, the XPS survey scan (Figure S2) showed significant peaks at 295, 550, and 991 eV, representing carbon (C 1s) and oxygen (O 1s and O KLL) species. The C 1s narrow scan (Figure 2A) presented binding peaks at 284.6, 285.8, 287.1, and 288.7 eV, which correlated to C–C, C–O, C=O, and O–C=O species.³⁶ The O 1s narrow scan (Figure 2B) displayed peaks at 531.8 and 533.3 eV, which were associated with C–O and C–O–C bonds in the GO structure. For the CIMMO/rGO composite, the wide scan exhibited similar binding peaks as observed from the GO. However, an additional peak was noticed from the O 1s narrow scan at 530.3 eV, representing the Metal–O binding species.^{37,38} The peak intensities at 533.7 and 531.6 eV, which indicated the presence of C–O–C and C–O species, were significantly reduced compared to GO.³⁶ The reduction in signal intensity from the functionalities could be attributed to a partial reduction reaction during the hydrothermal treatment for the composite's production. Figure 2C shows a narrow scan for Cu 2p of the composite, indicating Cu(0) and CuO/Cu₂O forms as major copper species. The Cu 2p_{3/2} narrow scan provides peaks at 933.4 and 935.1 eV, which were ascribed to Cu₂O/Cu³⁹ and CuO species.⁴⁰ The Cu 2p_{1/2} scan revealed binding energy peaks at 953.1 and 954.7 eV, corresponding to the CuO species. Two binding energy peaks for the Cu²⁺ satellites were identified at 942.2 and 962.5 eV, indicating the formation of copper ferrite alloys, such as Cu₂O–CuFe₂O₄.⁴¹ The interaction between Cu²⁺ and CIP is promoted by complexation with metal ions.⁴² The Fe 2p narrow scan (Figure 2D) displayed a firm peak that corresponded to Fe 2p_{3/2} at 710.9 eV. The peak represented the Fe²⁺/Fe³⁺ species in the composite.³³ It has been reported in the literature that the combination of Cu⁺/Cu²⁺ and Fe²⁺/Fe³⁺ assists in the redox reactions and could be a factor for the synergic effects between CIMMO/rGO and CIP.⁴³

2.1.6. Brunauer–Emmett–Teller (BET) Surface Area and Pore Volume Analysis. The Barrett–Joyner–Halenda (BJH) pore diameter and the pore volume of the GO and composites are shown in Figure 3A. GO had a surface area of $21.63 \text{ m}^2 \text{ g}^{-1}$, a pore diameter of 3.94 nm, and a pore volume of $0.07 \text{ cm}^3 \text{ g}^{-1}$ (Figure 3B). The 0.25:0.00:1.00 CIMMO/rGO provided a 37% increment in BET surface ($29.64 \text{ m}^2 \text{ g}^{-1}$) but an equivalent pore size (3.93 nm) and pore volume ($0.11 \text{ cm}^3 \text{ g}^{-1}$) compared to GO. The 0.00:0.25:1.00 CIMMO/rGO

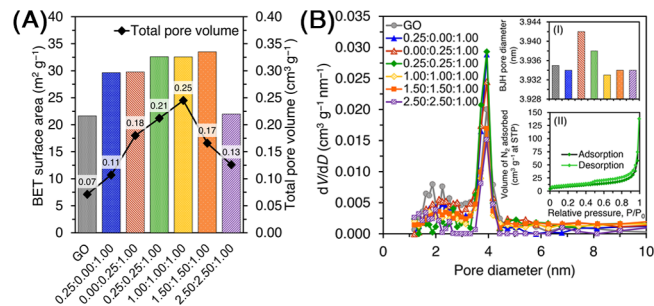


Figure 3. BET surface area and BJH pore diameter (A); pore volume distributions of composites (B) and N₂ adsorption–desorption isotherms of the 0.25:0.25:1.00 CIMMO/rGO (B, Inset).

showed an increased BET surface ($29.77 \text{ m}^2 \text{ g}^{-1}$) with an equivalent pore size (3.94 nm) and pore volume ($0.18 \text{ cm}^3 \text{ g}^{-1}$). The 0.25:0.25:1.00, 1.00:1.00:1.00, and 1.50:1.50:1.00 CIMMO/rGO composites yielded surface areas of 32.61, 32.58, and $33.52 \text{ m}^2 \text{ g}^{-1}$, pore sizes of 3.94, 3.94, and 3.93 nm, and pore volumes of 0.21, 0.25, and $0.17 \text{ cm}^3 \text{ g}^{-1}$, respectively. The 2.50:2.50:1.00 CIMMO/rGO presented a surface area of $22.50 \text{ m}^2 \text{ g}^{-1}$, a pore size of 3.93 nm, and a pore volume of $0.13 \text{ cm}^3 \text{ g}^{-1}$. The BET results agreed with the XRD results as the increased BET surface area and pore volume were attributable to the incorporation of CIMMO on GO. The pore sizes remained relatively constant with regard to the metal/metal oxide decoration, suggesting a transformation of the larger pores of the composites to deeper and narrower pores. This phenomenon was discontinued for 1.50:1.50:1.00 and 2.50:2.50:1.00 CIMMO/rGO as surface areas and pore volumes both decreased. The decrease could be attributed to the overdeposition of metal/metal oxide on the rGO structure. The N₂ adsorption–desorption isotherms (Figure 3B, Inset) obtained from the 0.25:0.25:1.00 CIMMO/rGO indicated a type-IV isotherm with a broad H4 hysteresis loop according to the recommendation of the International Union of Pure and Applied Chemistry (IUPAC). The isotherm demonstrated the initial formation of monolayer–multilayer adsorption in the mesopores, followed by hysteresis capillary condensation inside the pores. The H4 hysteresis loop was associated with an adsorbent with slit-shaped mesopores such as interfaces between CIMMO nanoparticles and CIMMO and rGO in the composite.

2.2. Electrochemical Characteristics of CIMMO/rGO/GCE.

2.2.1. Determination of the Electroactive Surface Area. The electrochemical characteristics of the modified electrodes were investigated using the cyclic voltammetry (CV) technique in a solution containing ferri/ferrocyanide redox mediator ($[\text{Fe}(\text{CN})_6]^{3-/4-}$) (Figure 4A). Experiments were conducted in a closed chamber, where the three electrodes were employed in a quartz cell and operated with or without light illumination. The effective surface area of a modified electrode was determined using the Randles–Sevcik equation (eq 1)

$$I_p = 2.69 \times 10^5 AD^{1/2} n^{3/2} \nu^{1/2} C \quad (1)$$

where I_p is the peak current, A is the electroactive area (cm^2), D is the diffusion coefficient ($4.0 \times 10^{-6} \text{ cm}^2 \text{ s}^{-1}$), n is the number of electrons, ν is the scan rate (V s^{-1}), and C is the concentration of $[\text{Fe}(\text{CN})_6]^{3-/4-}$ (mol cm^{-3}). Without light illumination, the area was 0.04 cm^2 for a bare glassy carbon electrode (GCE) but increased to 0.08 cm^2 for a GO-modified GCE. The 0.25:0.25:1.00 CIMMO/rGO/GCE displayed an

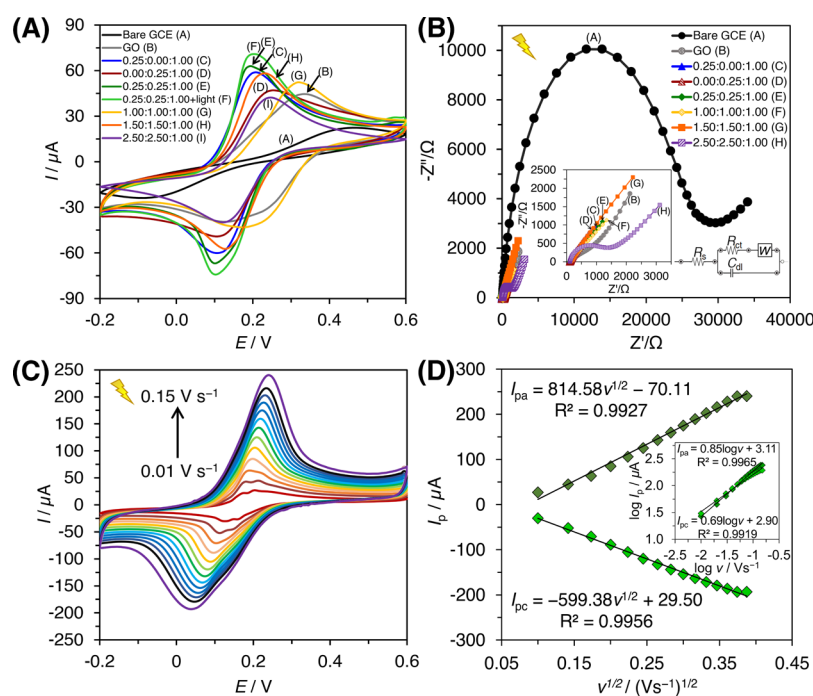


Figure 4. CV of the modified electrodes in $[\text{Fe}(\text{CN})_6]^{3-/4-}$ redox mediator (A); EIS Nyquist plots of the modified electrodes (0.1–100,000.0 Hz) (B) and the Randles equivalent circuit (B, Inset); CV plot of 0.25:0.25:1.00 CIMMO/rGO/GCE (0.01–0.15 V s^{-1} scan rate) (C); I_p vs $\nu^{1/2}$ plot (D) and $\log I_p$ vs $\log \nu$ plot (D, Inset) ($n = 3$).

area of 0.11 and 0.12 cm^2 in the absence and presence of light illumination, respectively. The electroactive areas for 0.25:0.00:1.00, 0.00:0.25:1.00, 1.00:1.00:1.00, 1.50:1.50:1.00, and 2.50:2.50:1.00 CIMMO/rGO/GCE were 0.10, 0.08, 0.10, 0.10, and 0.07 cm^2 , respectively. The areas per gram of catalyst (g_{CAT}) for GO/GCE and 0.25:0.00:1.00, 0.00:0.25:1.00, 0.25:0.25:1.00, 1.00:1.00:1.00, 1.50:1.50:1.00, and 2.50:2.50:1.00 CIMMO/rGO/GCE were 5.90, 6.90, 5.87, 7.70, 6.97, 6.95, and 4.98 $\text{m}^2 g_{\text{CAT}}^{-1}$, respectively. The electroactive area of the composite was 2.5 times less than that of the BET surface area, which could be attributed to parts of the composite pores not being electroactive or reachable by the electrolyte.

2.2.2. Electrochemical Impedance Spectroscopy (EIS). EIS was used to study the electrochemical characteristics of the composite electrode in the $[\text{Fe}(\text{CN})_6]^{3-/4-}$ redox mediator. The data were fitted by using an equivalent circuit function on the electrochemistry workstation. The notation C_{dl} denotes the double-layer capacitance, R_s denotes the electrolyte resistance, W denotes the Warburg impedance, and R_{ct} denotes the electron transfer resistance obtained from the semicircular diameter of the impedance. The simulated circuit connected R_s in parallel with C_{dl} , R_{ct} , and W . R_s was relatively constant for all of the tested samples as the same electrolyte composition was used. The Nyquist plots (Figure 4B) showed an R_{ct} of 26,334.39 Ω for the bare GCE but only 63.69 Ω for the GO/GCE. The R_{ct} of the 0.00:0.25:1.00 CIMMO/rGO composite was even lower, equaling 4.73 Ω due to improved charge transfer ability and electroactivity from CIMMO and rGO.²⁴ The R_{ct} decreased to 1.33, 2.60, and 3.23 Ω for the 0.25:0.25:1.00, 1.00:1.00:1.00, and 1.50:1.50:1.00 CIMMO/rGO composites, respectively. The 2.50:2.50:1.00 CIMMO/rGO exhibited an R_{ct} of 1,198.81 Ω , which was in agreement with the lessened electroactive surface areas noticed in the previous test. The results indicated that 0.25:0.25:1.00

CIMMO/rGO gave the lowest R_{ct} with the highest electroconductivity.

2.2.3. Electrochemical Characteristics of the Modified Electrode. The electroactivity of the composite was studied by using a cyclic voltammogram in the $[\text{Fe}(\text{CN})_6]^{3-/4-}$ medium (Figure 4C). The 0.25:0.25:1.00 CIMMO/rGO/GCE was employed in the electrochemical cell and illuminated. The applied potential was scanned within a -0.2 to 0.6 V window with a scan rate varying from 0.01 to 0.15 V s^{-1} . The CV curve provided redox potential peaks at 0.03 (reduction) and 0.20 V (oxidation), which tended to shift for a higher scan rate. The shift in the peaks suggested irreversible redox reactions at the working electrode. A plot of anodic peak current (I_{pa}) versus scan rate ($\nu^{1/2}$) (Figure 4D) revealed the correlation of I_{pa} (μA) = $814.58 \nu^{1/2} (\text{V s}^{-1})^{1/2} - 70.11$, with $R^2 = 0.9927$. The cathodic current peak (I_{pc}) correlation was I_{pc} (μA) = $-599.38 \nu^{1/2} (\text{V s}^{-1})^{1/2} + 29.50$, with $R^2 = 0.9956$. The $\log I_p$ versus $\log \nu$ plots revealed a slope of 0.85 and 0.69 for $I_{\text{pc}}-\nu$ and $I_{\text{pa}}-\nu$, respectively. The slopes fell within 0.5–1.0 windows, addressing the combined adsorption and diffusion-controlled mass transport.⁴⁴ The peak potential (E_p) follows the correlation from eq 2⁴⁵:

$$E_p = A + \frac{2.303RT}{(1-\alpha)nF} \log \nu \quad (2)$$

where A is a constant related to the formal electrode potential (E_0), α is the transfer coefficient ($\alpha = 0.5$) representing the effect of electrochemical potential, n is the number of electrons involved in the rate-controlling step, and R , T , and F are the gas constant, temperature, and Faraday constant, respectively. The n values were determined to be 0.6 and -0.8 for anodic and cathodic reactions, suggesting one proton and one electron transfer behavior at the electrode, which was consistent with the results of previous studies.⁴⁶ The composite displayed a magnetic property as it was attracted easily by an external

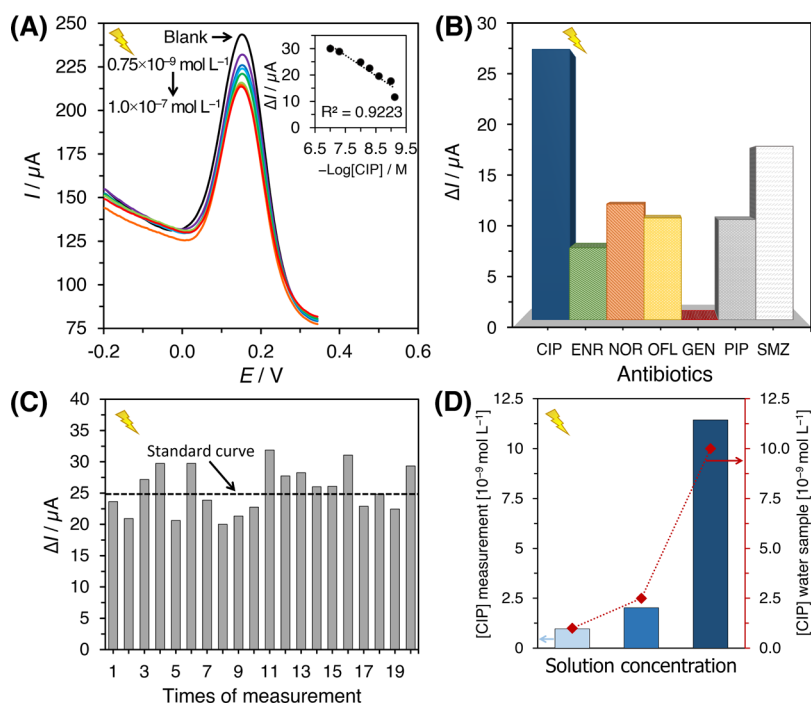


Figure 5. DPV curves corresponding to CIP concentrations (A); ΔI vs $-\text{Log}[\text{CIP}]$ ($n = 10$) (A, Inset); selectivity of the sensor against CIP and other antibiotics (B); sensing responses of a single sensor to $1.0 \times 10^{-8} \text{ mol L}^{-1}$ CIP (C); and measurements at different concentrations of CIP in spiked actual water samples with the 0.25:0.25:1.00 CIMMO/rGO/GCE sensor (D).

Table 1. Comparative Analysis of the 0.25:0.25:1.00 CIMMO/rGO Sensor and Other Reported CIP Sensors

sensitive element	mode of detection	supporting electrolyte	pH of the supporting electrolyte	linearity range ($\mu\text{mol L}^{-1}$)	limit of detection ($\mu\text{mol L}^{-1}$)	ref
Au/C ₃ N ₄ /GN/GCE	SWV	PBS	7.0	0.6–120.0	0.42	54
Ch-AuMIP/GCE	DPV	PBS and K ₃ Fe(CN) ₆	7.4	1.0–100.0	0.21	55
TiO ₂ /PVA/GCE	DPV	PBS	7.0	10.0–120.0	0.04	49
Co-MOFs/PLA/GCE	DPV	PBS	7.0	0.5–150.0	0.017	56
MgFe ₂ O ₄ -MWCNTs/GCE	CV	PBS	3.0	0.10–1000.0	0.01	57
NH ₂ -UiO-66/rGO/GCE	ASV	PBS	4.0	0.02–1.0	0.00667	58
Fe@g-C ₃ N ₄ /PGE	DPV	PBS	7.0	0.001–1.0	0.0054	59
CIMMO/rGO/GCE	DPV	PBS and [Fe(CN) ₆] ^{3-/4-}	6.5	0.00075–0.10	0.00047	this study

magnetic field (Figure S3A), which suggested a strong electroactivity of the material.⁴⁷

2.3. CIP Detection Experiments. **2.3.1. Effect of Solution pH on Sensing Responses.** For the CIP detection experiments, we used phosphate buffer solution (PBS) containing $1.0 \times 10^{-6} \text{ mol L}^{-1}$ CIP and evaluated the influence of solution pH within a pH window of 4–8 (Figure S3B). The tests were conducted in DPV mode, with potential scanning from +0.4 to +1.4 V. As the solution pH increased from 4 to 6, the electrochemical responses increased from 150 to 165 μA . The signal stabilized for a CIP solution pH of 6.5 but dropped significantly at 8.0 due to proton scarcity in the alkaline solution.¹¹ The correlation was linear in the pH 4–8 range (eq 3), showing a regression (R^2) of 0.95.

$$E_p \text{ (V)} = -0.1007\text{pH} + 1.6039 \quad (R^2 = 0.95) \quad (3)$$

The slope was determined to be $-0.1007 \text{ V pH}^{-1}$, deviating from the theoretical Nernstian value of -0.059 V pH^{-1} . The deviation could be attributable to charge losses to other active radicals and differences in experimental conditions, such as electrolyte concentration and temperature.⁴⁸ Based on the

findings, a pH 6.5 solution was selected for subsequent investigations.

2.3.2. CIP Detection. The 0.25:0.25:1.00 CIMMO/rGO/GCE was incubated with the CIP solution at pH 6.5 for 1 min and then positioned in the electrochemical cell for the CIP measurement. The modified GCE was operated in DPV mode and exhibited sensitivity to CIP within a concentration range of 0.75×10^{-9} – $1.0 \times 10^{-7} \text{ mol L}^{-1}$ (Figure 5A). The current signal (ΔI) peaked at 0.16 V. We conducted a study to detect CIP concentrations across a wide range, which examined frequent measurements made at low concentrations and a rapid increase at high concentrations. The current signal demonstrated nonlinear behavior in response to the CIP concentrations and linear behavior with respect to the logarithmic CIP concentration ($\log[\text{CIP}]$). The equation was $\Delta I \text{ (}\mu\text{A)} = 7.68 \log[\text{CIP}] \text{ (mol L}^{-1}\text{)} + 85.01$, with an R^2 of 0.9223 ($n = 10$), where ΔI denotes the difference in peak current in the absence and presence of CIP. The LOD was determined to be $4.74 \times 10^{-10} \text{ mol L}^{-1}$, based on the relationship $\text{LOD} = 3.3 \text{ SD/S}$,⁴⁹ where SD denotes the standard deviation of the intercept and S denotes the slope of the calibration plot (Figure 5A, inset). The logarithmic

correlation between the electrochemical current and [CIP] suggested an indirect interaction between CIP and the composite. The peak intensity decreases as the CIP either competes with the mediator in withdrawing electrons from the working electrode, adsorbs onto and passivates the electrode, or interacts with the active mediator. We compared CIP sensing results from the composite sensor to the results of other reports (Section 2.5 and Table 1). Our results provided a low detection limit ($0.00047 \mu\text{mol L}^{-1}$) and a wide linearity range ($0.00075\text{--}0.10 \mu\text{mol L}^{-1}$). The 0.25:0.25:1.00 CIMMO/rGO/GCE sensor was selected for the cross-sensitivity (selectivity) test, as demonstrated in Figure 5B. The sensor was introduced to two groups of antibiotics: molecules structurally similar to CIP and molecules not structurally related at $1.0 \times 10^{-7} \text{ mol L}^{-1}$. The former group included enrofloxacin (ENR), norfloxacin (NOR), and ofloxacin (OFL), and the latter included gentamicin (GEN), piperacillin sodium salt (PIP), and sulfamethoxazole (SMZ). The sensor exhibited an ΔI value of $27.8 \mu\text{A}$ for CIP. The ΔI_{CIP} values were 3.76, 2.34, 2.66, 2.70, and 1.64 times higher than the responses for ENR, NOR, OFL, PIP, and SMZ, respectively, with no significant response against GEN.

2.3.3. Assessment of the Reusability, Reproducibility, and Stability of the Sensor. The reusability of the sensor was determined using the same modified electrode for successive DPV detection. The single modified electrode was introduced to $1.0 \times 10^{-8} \text{ mol L}^{-1}$ CIP in 0.05 mol L^{-1} PBS and analyzed in the $[\text{Fe}(\text{CN})_6]^{3-/4-}$ medium (Figure 5C). The electrode was rinsed in DI water for 1.0 min and reintroduced into the CIP solution. This process was repeated 20 times, and the SD and relative standard deviation (RSD) for the measurements were determined to be 3.7 and 14.5%, respectively. The surface morphology of the CIMMO/rGO composite was analyzed by field emission-scanning electron microscopy (FE-SEM). The SEM showed no significant change in CIMMO/rGO surface morphology from before to after one round of CV analysis (Figure S4A,B). The variations in sensing readouts could be attributed to the composite film damage caused by the surface tension of the solutions. We believe that the issue could be alleviated by coating another porous membrane, such as Nafion, on top of the composite film to promote film adhesion to the GCE and improve the physical strength. The reproducibility and stability of 0.25:0.25:1.00 CIMMO/rGO were evaluated in a mediator (Figure S5). The five electrodes, prepared using the same method, demonstrated good reproducibility with an RSD of their response currents of 1.10%. The stability of a single electrode was also assessed, yielding an RSD of 0.60%. Consequently, 0.25:0.25:1.00 CIMMO/rGO demonstrates commendable reproducibility and stability.

2.3.4. CIP Detection in Surface Water Samples. The process used for water sample preparation is explained in the Supporting Information. Basic properties, including pH, temperature during sample collection, dissolved oxygen, conductivity, and salinity, were tested and are presented in Table S1. CIP was added to the surface water, creating solutions of 1.0×10^{-9} , 2.5×10^{-9} , and $10.0 \times 10^{-9} \text{ mol L}^{-1}$ CIP for the measurements. The readout values from the composite sensor were 1.0×10^{-9} , 2.0×10^{-9} , and $11.4 \times 10^{-9} \text{ mol L}^{-1}$, respectively, with $P > 0.05$ in the *t*-test analysis (Figure 5D). The deviations of the measurement were determined using the equation [(Sensor readout) – (Actual

concentration)]/[Actual concentration] $\times 100$ and were from 14 to 19% (Table S2).

2.4. Proposed Reaction Mechanisms. The reaction mechanisms for the composite sensor rely on the types of metals, surface morphology, and interaction/reaction with the targeted analyte (Figure 6). As the CIMMO/rGO composite is

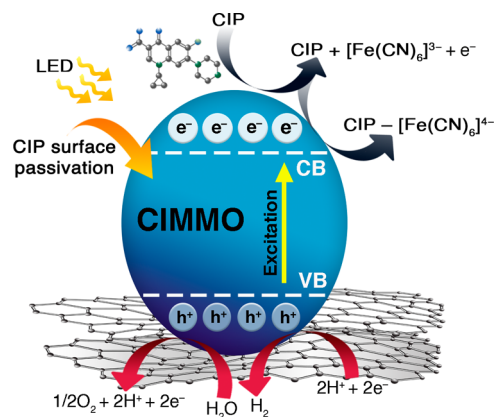
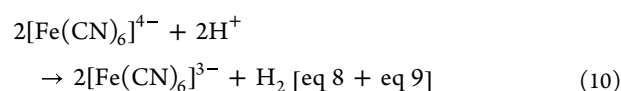
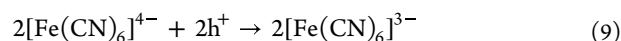
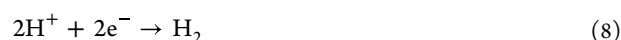
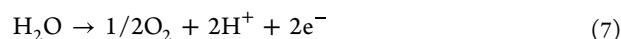
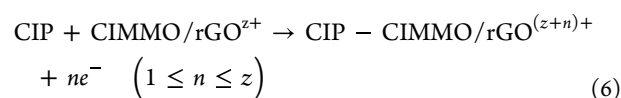
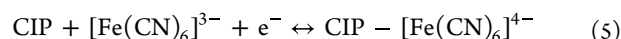


Figure 6. Schematic diagram showing proposed mechanisms for the indirect interactions of CIMMO/rGO with CIP.

illuminated, photoinduced electrons and holes (h^+) are generated and repositioned at the conduction band (CB) and valence band (VB), respectively (eq 4). The electron–hole separation occurs with partial assistance from the applied potential at the electrode. CIP oxidation means that electrons withdraw from the working electrode, which should result in a higher anodic current. However, the response from the DPV technique decreased as the CIP concentration increased, suggesting diminishing electron transfer at the working electrode. The $[\text{Fe}(\text{CN})_6]^{3-}$ was electrochemically reduced to $[\text{Fe}(\text{CN})_6]^{4-}$, establishing the redox couple $[\text{Fe}(\text{CN})_6]^{3-}/[\text{Fe}(\text{CN})_6]^{4-}$. The reduction in current could be attributed to the interactions of CIP and $[\text{Fe}(\text{CN})_6]^{3-/4-}$ (eq 5), which decelerated the charge transfer or CIP adsorption that partly passivated the CIMMO/rGO electrode (eq 6).⁵⁰ It is worth noting that both phenomena involve an equal number of electron and proton transfers (Section 2.2.3 and Figure 4D), indicating the indirect interactions between the CIP and the working electrode.



The reduction reaction completing the redox reaction occurs at the composite CB. It involves water (H_2O) dissociation into

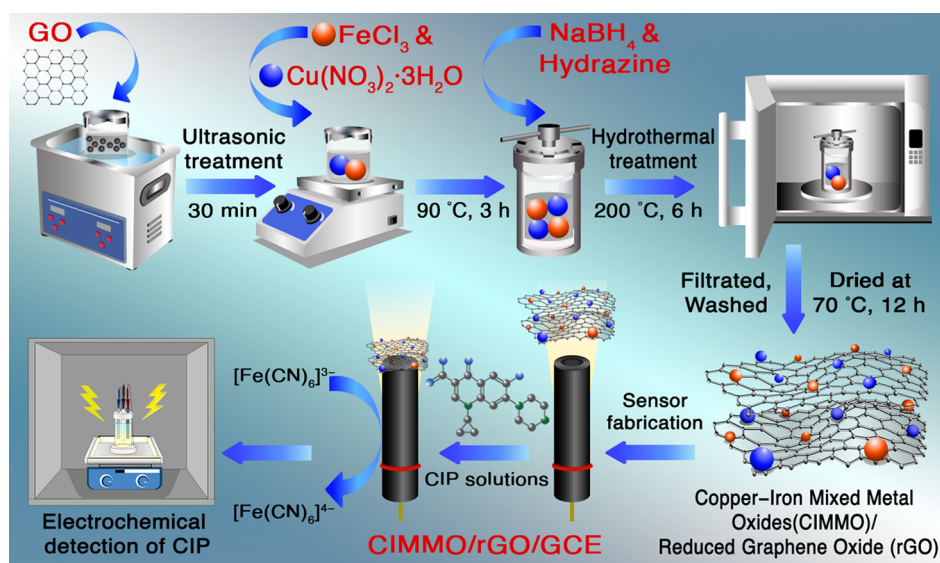


Figure 7. Diagram showing the CIMMO/rGO/GCE fabrication process and CIP detection.

oxygen, electrons, and protons (eq 7), giving two electrons ($n = 2$) for the electrochemical reaction.⁵¹ The protons can couple to other electrons to produce H_2 (eq 8). Photoinduced holes (h^+) interact with $[Fe(CN)_6]^{3-}$ mediator, yielding $[Fe(CN)_6]^{4-}$ (eq 9). The total reaction (eq 8 + eq 9) is presented in eq 10.⁵² The combination of mixed metal oxides in the composite structures resulted in a synergistic effect, in which the iron oxides contributed mainly as the photoelectrocatalyst.⁵³ As the composite was illuminated, the electron energy was enhanced from the VB to the CB level. The CB electrons crossed the copper–iron interfaces, reaching the copper metal oxide matrix with an effective electron transfer ability. The CIP accepted photoinduced electrons from the copper oxide sites (CB), while the photoinduced h^+ were withdrawn from the VB site of iron and copper oxides. The synergy phenomenon enhanced the number of photoinduced electrons by reducing the rate of electron–hole recombination, promoting the photoactivity of the composite material.

2.5. Comparative Analysis between the CIMMO/rGO Electrochemical Sensor and Other Reported Sensors.

We compared the 0.25:0.25:1.00 CIMMO/rGO/GCE sensor with other reported sensors (Table 1). Yuan et al.⁵⁴ synthesized Au nanoparticles/carbon nitride/graphene (Au/C₃N₄/GN/GCE) and cast it onto GCE. The electrode, operated in square wave voltammetry (SWV) mode, exhibited a linear detection window from 0.60 to 120.0 $\mu\text{mol L}^{-1}$ CIP and an LOD of 0.42 $\mu\text{mol L}^{-1}$. Surya et al.⁵⁵ combined gold nanoparticles and chitosan to create MIP on a GCE (Ch-AuMIP/GCE). The MIP electrode was operated in DPV mode and at concentrations of 1.0–100.0 $\mu\text{mol L}^{-1}$ CIP. The LOD value was reported as 0.21 $\mu\text{mol L}^{-1}$. Zhao et al.⁴⁹ coated TiO₂ and poly(vinyl alcohol) onto a GCE (TiO₂/PVA/GCE) using a dip-coating technique. They obtained a broad and good detection response from CIP with a linear range of 10.0–120.0 $\mu\text{mol L}^{-1}$ and LOD of 0.04 $\mu\text{mol L}^{-1}$. Yahyapour et al.⁵⁶ synthesized cobalt (Co)-metal-organic frameworks (MOFs) and polylactic acid nanofiber on GCE (Co-MOFs/PLA/GCE). The Co-MOF/PLA/GCE had a linear response range to CIP of 0.5–150.0 $\mu\text{mol L}^{-1}$ and an LOD of 0.017 $\mu\text{mol L}^{-1}$. Ensafi et al.⁵⁷ prepared magnesium ferrite (MgFe₂O₄)

nanoparticle-decorated multiwalled carbon nanotubes (MWCNTs) on GCE (MgFe₂O₄-MWCNTs/GCE) and studied the electrode using the CV technique. It showed good detection within a 0.10–1000.0 $\mu\text{mol L}^{-1}$ CIP range with an LOD of 0.01 $\mu\text{mol L}^{-1}$. Fang et al.⁵⁸ prepared Zr(IV)-based MOF and rGO composite (NH₂-UiO-66/rGO/GCE). The composite was fabricated with an electrochemical sensor that relied on anodic stripping voltammetry (ASV) mode. The sensor detected CIP within a linear range of 0.02–1.0 $\mu\text{mol L}^{-1}$ and had an LOD of 0.00667 $\mu\text{mol L}^{-1}$. Vedhavathi et al.⁵⁹ modified a pencil graphite electrode (PGE) with an iron-decorated graphitic carbon nitride composite (Fe@g-C₃N₄/PGE). Operated in a DPV mode, the sensor showed a CIP linear detection range of 0.001–1.0 $\mu\text{mol L}^{-1}$ and an LOD of 0.0054 $\mu\text{mol L}^{-1}$. Compared to sensors described in previous reports, the composite sensor examined in this study demonstrated an enhanced efficacy for CIP detection, exhibiting an extensive linear range and a notably low LOD.

3. CONCLUSIONS

We synthesized CIMMO/rGO composites following a one-step hydrothermal technique and coated them as a thin film on a GCE electrode. The 0.25:0.25:1.00 CIMMO/rGO/GCE demonstrated outstanding performance as an electrochemical sensor for CIP detection, producing the equation of $\Delta I (\mu\text{A}) = 7.68 \log[\text{CIP}] (\text{mol L}^{-1}) + 85.01$ (R^2 of 0.9223) for 0.75×10^{-9} – 1.0×10^{-7} mol L⁻¹ CIP. The LOD was 4.74×10^{-10} mol L⁻¹. The composite sensor exhibited acceptable selectivity to CIP, providing responses to CIP that were 1.6 to 3.8 times higher than responses to other antibiotics. The sensor also showed good reusability and sufficient responses to CIP in actual water samples.

4. METHODOLOGY

4.1. Chemicals and Reagents.

All chemicals were of analytical grade and used with no additional purification. The aqueous solutions were prepared with UPW from a Millipore Milli-Q system (18.2 M Ω -cm). Graphite flakes (10 mesh size) were purchased from Alfa Aesar (USA). Copper nitrate trihydrate (Cu(NO₃)₂·3H₂O) (Qrec, New Zealand), potassium permanganate (KMnO₄) (Ajax Finechem Pty, Ltd.,

Australia), iron(III) chloride (FeCl_3) (Carlo Erba, Italy), and sodium nitrate (NaNO_3) (Fluka Chemika, Switzerland) were used as received. Hydrazine sulfate ($\text{H}_2\text{N}-\text{NH}_2\cdot\text{H}_2\text{SO}_4$) (AppliChem GmbH, Germany) and sulfuric acid (H_2SO_4) (RCI Labscan, Ltd., Thailand) were reagent grade and used with no further treatment. CIP, ENR, NOR, OFL, SMZ, and PIP were HPLC grade and purchased from Sigma-Aldrich (USA). GEN was purchased from Himedia Laboratories Pvt. Ltd. (India). Potassium hexacyanoferrate (III) ($\text{K}_3\text{Fe}(\text{CN})_6$), potassium hexacyanoferrate (II) trihydrate ($\text{K}_4\text{Fe}(\text{CN})_6\cdot 3\text{H}_2\text{O}$), and potassium chloride (KCl) were obtained from Sigma-Aldrich (USA). Ethanol ($\text{C}_2\text{H}_5\text{OH}$), 30% hydrogen peroxide (H_2O_2), hydrochloric acid (HCl), sodium borohydride (NaBH_4), and sodium hydroxide (NaOH) were purchased from Merck, Germany. Dipotassium phosphate (K_2HPO_4) and potassium phosphate (KH_2PO_4) (Merck, Germany) were used in the preparation of 0.05 mol L^{-1} PBS.

4.2. GO Synthesis. GO was chemically synthesized following a chemical exfoliation method.⁶⁰ We mixed 2.0 g of graphite flakes with 1.0 g of NaNO_3 and 50.0 mL of H_2SO_4 and stirred the mixture for 2 h at 0 °C. The KMnO_4 oxidizer (7.3 g) was gradually poured into the mixture during the stirring. The mixture was moved to ambient conditions and stirred for 2.5 h before a solution of 55.0 mL of UPW and 7.0 mL of H_2O_2 was added to terminate the oxidation reaction. The powder was rinsed with 3% HCl and UPW to remove excess manganese residuals. GO was heated in a vacuum oven at 60 °C for 24 h and stored in a desiccator until used.

4.3. Synthesis of the CIMMO/rGO Composite. The CIMMO/rGO composites were synthesized using a hydrothermal technique modified from the method presented by Yang et al.⁶¹ GO suspension was prepared in distilled water with a known amount of $\text{Cu}(\text{NO}_3)_2\cdot 3\text{H}_2\text{O}$ and FeCl_3 , which was added with stirring at 90 °C for 3 h (Figure 7). The mixture was cooled to ambient temperature and mixed with hydrazine before being transferred to a 100 mL Teflon-lined autoclave. The autoclave was held at 200 °C for 6 h. The composite powder was rinsed several times using UPW and dried at 70 °C to obtain fine particles. GO was introduced to hydrazine with heat during composite production and was reduced to rGO in the CIMMO/rGO composites. The composite was prepared at various Cu:Fe:GO ratios, among which the ratio of 0.25:0.00:1.00 indicates a composite that was synthesized using 0.25 w/w copper mixed metal oxide precursor/GO, 0.00 w/w iron mixed metal oxide precursor/GO, and 1.00 w/w GO/GO. Composites with other intermediate ratios, including 0.00:0.25:1.00, 0.25:0.25:1.00, 1.00:1.00:1.00, 1.50:1.50:1.00, and 2.50:2.50:1.00, were also synthesized and characterized.

4.4. Fabrication of CIMMO/rGO/GCE. The composite powder was dispersed in UPW (1.0 mg mL^{-1}) via ultrasonication at 59 W, creating the suspension. The GCE was polished sequentially with 1.0, 0.3, and 0.05 μm alumina slurries, followed by treatment with 1:1 (v/v) HNO_3 /UPW, ethanol, and UPW. The cleansed surface was dried in a stream of nitrogen. A 10- μL drop of CIMMO/rGO suspension was cast on the GCE and warmed at 60 °C for 15 min to dry. The composite film was uniform at 1.42 μg of mm^{-2} .

4.5. Electrochemical Measurements. A 3-electrode electrochemical quartz cell employed a GCE (working electrode) with an Ag/AgCl reference electrode and platinum mesh (counter electrode). Electrochemical signals were monitored through a portable PalmSens4 analyzer under

intense irradiation of four light-emitting diodes (LEDs) (3W, 320 lm/bulb). The sensors were operated in CV mode with a -0.2 to $+0.6$ V potential window and 0.05 V s^{-1} scan rate for 10 cycles. The sensor was used in DPV mode, with the application of a wide potential window of -0.2 to $+0.6$ V, step potential (E_{step}) of 0.005 V, pulse potential (E_{pulse}) of 0.06 V, pulse time (t_{pulse}) of 0.02 s, and scan rate of 0.05 V s^{-1} . We used 5.0×10^{-3} mol L^{-1} $[\text{Fe}(\text{CN})_6]^{3-/4-}$ redox mediator in 0.1 mol L^{-1} KCl at pH 6.5 as a medium for electrochemical measurements. EIS measurements were performed at 0.1 to 100,000.0 Hz with a DC potential of $+0.15$ V and a set amplitude (E_{ac}) of $+0.006$ V. The EIS analysis was carried out using a modeled equivalent circuit.

4.6. Material Characterizations. μXRF (XGT-9000, Horiba, Ltd., Japan) was utilized to determine the mass composition of the samples. To analyze crystal structures, XRD (D2 Phaser, Bruker, Germany, $\text{CuK}\alpha$ radiation) was performed with a scanning range from 5° to 90° (2θ) at a step size of 0.02° and a scanning rate of 2° min^{-1} . FT-IR analyses were recorded on a Nicolet iS50 spectrometer in the 400 – 4000 cm^{-1} range. BET analysis (Quantachrome ASIQwin, Automated gas sorption analyzer instrument, version 5.23) was used for specific surface area and pore volume analysis. Physical morphologies of the samples were observed by using TEM (FEI, Tecnai G2 20) operated at 200 kV and FE-SEM (JEOL Ltd., JSM-7800F Prime instrument, Tokyo, Japan). Surface compositions and chemical binding energies were studied by using XPS (Kratos AXIS Ultra DLD, Kratos, UK), utilizing a monochromatized Al $\text{K}\alpha$ radiation source.

■ ASSOCIATED CONTENT

Supporting Information

The Supporting Information is available free of charge at <https://pubs.acs.org/doi/10.1021/acsomega.3c06705>.

Additional information as noted in the text; preparation of actual water samples; basic properties of surface water; actual water sample testing and statistical analysis; size distribution histograms; XPS survey spectra; magnetic characteristic of the various ratio of CIMMO/rGO composite and the effect of medium pH on sensing responses; FE-SEM images; and the reproducibility and the stability of sensor (PDF)

■ AUTHOR INFORMATION

Corresponding Authors

Sira Srinives – Nanocomposite Engineering Laboratory (NanoCEN), Department of Chemical Engineering, Faculty of Engineering, Mahidol University, Nakhon Pathom 73170, Thailand; orcid.org/0000-0002-7890-1103; Phone: 66-2-8892138 ext 6101-3; Email: sira.sri@mahidol.edu

Suwanna Kitpati Boontanon – Graduate Program in Environmental and Water Resources Engineering, Department of Civil and Environmental Engineering, Faculty of Engineering, Mahidol University, Nakhon Pathom 73170, Thailand; Graduate School of Global Environmental Studies, Kyoto University, Kyoto 606-8501, Japan; Phone: 66-2-8892138 ext 6390; Email: suwanna.boo@mahidol.ac.th

Authors

Jedsada Chuiprasert – Graduate Program in Environmental and Water Resources Engineering, Department of Civil and Environmental Engineering, Faculty of Engineering, Mahidol

University, Nakhon Pathom 73170, Thailand; orcid.org/0000-0003-4507-7127

Narin Boontanon – Faculty of Environment and Resource Studies, Mahidol University, Nakhon Pathom 73170, Thailand

Chongrak Polprasert – Department of Civil Engineering, Faculty of Engineering, Thammasat University, Pathum Thani 12120, Thailand

Nudjarin Ramungul – National Metal and Materials Technology Center, National Science and Technology Development Agency, Pathum Thani 12120, Thailand

Apisit Karawek – Nanocomposite Engineering Laboratory (NanoCEN), Department of Chemical Engineering, Faculty of Engineering, Mahidol University, Nakhon Pathom 73170, Thailand

Complete contact information is available at:

<https://pubs.acs.org/10.1021/acsomega.3c06705>

Author Contributions

J.C.: conceptualization, methodology, data curation, visualization, formal analysis, and writing—original draft and editing; S.S.: conceptualization, supervision, methodology, resources, validation, writing—review and editing, and funding acquisition; N.B.: methodology and conceptualization; C.P.: conceptualization and supervision; N.R.: project administration and funding acquisition; A.K.: data curation and writing—original draft; and S.K.B.: conceptualization, supervision, formal analysis, methodology, validation, writing—reviewing and editing, and funding acquisition.

Notes

The authors declare no competing financial interest.

ACKNOWLEDGMENTS

This work was financially supported by the Royal Golden Jubilee (RGJ) Ph.D. program (Grant No. PHD/0051/2561) under the National Research Council of Thailand (NRCT). This work was also supported by the On-site Laboratory Initiative of the Graduate School of Global Environmental Studies, Kyoto University. Sira Srinives is grateful for the financial support from the MU Talent Program, Faculty of Engineering, Mahidol University. Special thanks to the Mahidol University Frontier Research Facility (MU-FRF) for instrumental support and the MU-FRF specialists Nawapol Udpuay, Dr. Suwilai Chaveanghong, and Chawalit Takoon for their assistance in the sample characterizations. Sira Srinives credited the individual development program (The MU talent), Faculty of Engineering, Mahidol University, for partial funding and contribution of sample characterizations to the Department of Chemical Engineering Central lab with assistance from Mr. Ruksong Yasachai and Mr. Chonlathon Kinkaw. Graham K. Rogers provided his contribution in editing.

ABBREVIATIONS

ABR, antibiotic resistance; ASV, anodic stripping voltammetry; BET, Brunauer–Emmett–Teller; BJH, Barrett–Joyner–Halenda; CB, conduction band; CIMMO, copper–iron mixed metal oxides; CIP, ciprofloxacin; Cu, copper; CV, cyclic voltammetry; DPV, differential pulse voltammetry; EBSD, electron backscatter diffraction mode; EIS, electrochemical impedance spectroscopy; ENR, enrofloxacin; Fe, iron; GC, gas chromatography; GCE, glassy carbon electrode; GEN,

gentamicin; GO, graphene oxide; HPLC–MS/MS, high-performance liquid chromatography coupled with mass spectrometry; IUPAC, International Union of Pure and Applied Chemistry; LEDs, light-emitting diodes; LOD, limit of detection; MIPs, molecularly imprinted polymers; MMWCNTs, magnetic multiwalled carbon nanotubes; MWCNTs, multiwalled carbon nanotubes; NOR, norfloxacin; OFL, ofloxacin; PBS, phosphate buffer solution; PGE, pencil graphite electrode; PIP, piperacillin sodium salt; rGO, reduced graphene oxide; R_{ct} , electron transfer resistance; RSD, relative standard deviation; SAED, selected area electron diffraction; SD, standard deviation; SMZ, sulfamethoxazole; SWV, square wave voltammetry; UPW, ultrapure water; VB, valence band

REFERENCES

- (1) Zhang, Q.; Jia, A.; Wan, Y.; Liu, H.; Wang, K.; Peng, H.; Dong, Z.; Hu, J. Occurrences of three classes of antibiotics in a natural river basin: association with antibiotic-resistant *Escherichia coli*. *Environ. Sci. Technol.* **2014**, *48* (24), 14317–14325.
- (2) Hairom, N. H. H.; Soon, C. F.; Mohamed, R. M. S. R.; Morsin, M.; Zainal, N.; Nayan, N.; Zulkifli, C. Z.; Harun, N. H. A review of nanotechnological applications to detect and control surface water pollution. *Environ. Technol. Innov.* **2021**, *24*, No. 102032.
- (3) Patel, M.; Kumar, R.; Kishor, K.; Mlsna, T.; Pittman, C. U., Jr; Mohan, D. Pharmaceuticals of emerging concern in aquatic systems: chemistry, occurrence, effects, and removal methods. *Chem. Rev.* **2019**, *119* (6), 3510–3673.
- (4) Al-Buriah, A. K.; Al-shaibani, M. M.; Mohamed, R. M. S. R.; Al-Gheethi, A. A.; Sharma, A.; Ismail, N. Ciprofloxacin removal from non-clinical environment: A critical review of current methods and future trend prospects. *J. Water Process. Eng.* **2022**, *47*, No. 102725.
- (5) Sinthuchai, D.; Boontanon, S. K.; Boontanon, N.; Polprasert, C. Evaluation of removal efficiency of human antibiotics in wastewater treatment plants in Bangkok. *Thailand. Water Sci. Technol.* **2016**, *73* (1), 182–191.
- (6) Tripathi, A.; Bonilla-Cruz, J. J. A. A. N. M. Review on Healthcare Biosensing Nanomaterials. *ACS Appl. Nano Mater.* **2023**, *6* (7), 5042–5074.
- (7) Nguyen, T. N. T.; Thi Pham, N.; Ngo, D.-H.; Kumar, S.; Cao, X. T. Covalently Functionalized Graphene with Molecularly Imprinted Polymers for Selective Adsorption and Electrochemical Detection of Chloramphenicol. *ACS Omega* **2023**, *8* (28), 25385–25391.
- (8) Wan, X.; Du, H.; Tuo, D.; Qi, X.; Wang, T.; Wu, J.; Li, G. UiO-66/Carboxylated Multiwalled Carbon Nanotube Composites for Highly Efficient and Stable Voltammetric Sensors for Gatifloxacin. *ACS Appl. Nano Mater.* **2023**, *6* (20), 19403–19413.
- (9) Li, G.; Wan, X.; Xia, Y.; Tuo, D.; Qi, X.; Wang, T.; Mehmandoust, M.; Erk, N.; He, Q.; Li, Q. Lamellar α -Zirconium phosphate nanoparticles supported on N-doped graphene nanosheets as electrocatalysts for the detection of levofloxacin. *ACS Appl. Nano Mater.* **2023**, *6* (18), 17040–17052.
- (10) Vu, O. T.; Nguyen, Q. H.; Nguy Phan, T.; Luong, T. T.; Eersels, K.; Wagner, P.; Truong, L. T. N. Highly Sensitive Molecularly Imprinted Polymer-Based Electrochemical Sensors Enhanced by Gold Nanoparticles for Norfloxacin Detection in Aquaculture Water. *ACS Omega* **2023**, *8* (3), 2887–2896.
- (11) Bagheri, H.; Khoshsafar, H.; Amidi, S.; Ardakani, Y. H. Fabrication of an electrochemical sensor based on magnetic multiwalled carbon nanotubes for the determination of ciprofloxacin. *Anal. Methods* **2016**, *8* (16), 3383–3390.
- (12) Li, G.; Qi, X.; Wu, J.; Wan, X.; Wang, T.; Liu, Y.; Chen, Y.; Xia, Y. Highly stable electrochemical sensing platform for the selective determination of pefloxacin in food samples based on a molecularly imprinted-polymer-coated gold nanoparticle/black phosphorus nanocomposite. *Food Chem.* **2024**, *436*, No. 137753.
- (13) Chuiprasert, J.; Srinives, S.; Boontanon, N.; Polprasert, C.; Ramungul, N.; Lertthanaphol, N.; Karawek, A.; Boontanon, S. K.

- Electrochemical Sensor Based on a Composite of Reduced Graphene Oxide and Molecularly Imprinted Copolymer of Polyaniline–Poly (*o*-phenylenediamine) for Ciprofloxacin Determination: Fabrication, Characterization, and Performance Evaluation. *ACS Omega* **2023**, *8* (2), 2564–2574.
- (14) Li, M.; Wang, H.; Wang, X.; Lu, Q.; Li, H.; Zhang, Y.; Yao, S. Ti₃C₂/Cu₂O heterostructure based signal-off photoelectrochemical sensor for high sensitivity detection of glucose. *Biosens. Bioelectron.* **2019**, *142*, No. 111535.
- (15) Yang, M.; Chen, Y.; Yan, P.; Dong, J.; Duan, W.; Xu, L.; Li, H. A photoelectrochemical aptasensor of ciprofloxacin based on Bi₂₄O₃₁Cl₁₀/BiOCl heterojunction. *Mikrochim. Acta* **2021**, *188* (9), 1–8.
- (16) Chen, M.; Xu, Y. Trace amount CoFe₂O₄ anchored on a TiO₂ photocatalyst efficiently catalyzing O₂ reduction and phenol oxidation. *Langmuir* **2019**, *35* (29), 9334–9342.
- (17) Gan, Y.; Zhang, M.; Xiong, J.; Zhu, J.; Li, W.; Zhang, C.; Cheng, G. Impact of Cu particles on adsorption and photocatalytic capability of mesoporous Cu@TiO₂ hybrid towards ciprofloxacin antibiotic removal. *J. Taiwan Inst. Chem. Eng.* **2019**, *96*, 229–242.
- (18) Pienutsa, N.; Yannawibut, K.; Phattharaphongmanee, J.; Thongantakul, O.; Srinives, S. Titanium dioxide-graphene composite electrochemical sensor for detection of hexavalent chromium. *Int. J. Miner. Metall. Mater.* **2022**, *29* (3), 529–535.
- (19) Sullivan, I.; Zoellner, B.; Maggard, P. A. Copper (I)-based p-type oxides for photoelectrochemical and photovoltaic solar energy conversion. *Chem. Mater.* **2016**, *28* (17), 5999–6016.
- (20) Gholivand, M. B.; Shamsipur, M.; Paimard, G.; Feyzi, M.; Jafari, F. Synthesis of Fe–Cu/TiO₂ nanostructure and its use in construction of a sensitive and selective sensor for metformin determination. *Mater. Sci. Eng., C* **2014**, *42*, 791–798.
- (21) Khalilzadeh, M. A.; Tajik, S.; Beitollahi, H.; Venditti, R. A. Green synthesis of magnetic nanocomposite with iron oxide deposited on cellulose nanocrystals with copper (Fe₃O₄@CNC/Cu): investigation of catalytic activity for the development of a venlafaxine electrochemical sensor. *Ind. Eng. Chem. Res.* **2020**, *59* (10), 4219–4228.
- (22) Alomair, N. A.; Al-Aqeel, N. S.; Alabbad, S. S.; Kochkar, H.; Berhault, G.; Younas, M.; Jomni, F.; Hamdi, R.; Ercan, I. The Role of the Ferroelectric Polarization in the Enhancement of the Photocatalytic Response of Copper-Doped Graphene Oxide–TiO₂ Nanotubes through the Addition of Strontium. *ACS Omega* **2023**, *8* (9), 8303–8319.
- (23) Fu, H.; Li, X.; Wang, J.; Lin, P.; Chen, C.; Zhang, X.; Suffet, I. M. Activated carbon adsorption of quinolone antibiotics in water: Performance, mechanism, and modeling. *J. Environ. Sci.* **2017**, *56*, 145–152.
- (24) Zhu, M.; Li, R.; Lai, M.; Ye, H.; Long, N.; Ye, J.; Wang, J. Copper nanoparticles incorporating a cationic surfactant-graphene modified carbon paste electrode for the simultaneous determination of gatifloxacin and pefloxacin. *J. Electroanal. Chem.* **2020**, *857*, No. 113730.
- (25) Daizy, M.; Tarafder, C.; Al-Mamun, M. R.; Liu, X.; Aly Saad Aly, M.; Khan, M. Z. H. Electrochemical detection of melamine by using reduced graphene oxide–copper nanoflowers modified glassy carbon electrode. *ACS. Omega* **2019**, *4* (23), 20324–20329.
- (26) Al-Nami, S. Y.; Alorabi, A. Q.; Al-Ahmed, Z. A.; Mogharbel, A. T.; Abumelha, H. M.; Hussein, M. A.; El-Metwaly, N. M. Superficial and Inkjet Scalable Printed Sensors Integrated with Iron Oxide and Reduced Graphene Oxide for Sensitive Voltammetric Determination of Lurasidone. *ACS Omega* **2023**, *8* (11), 10449–10458.
- (27) Shi, X.-M.; Wang, C.-D.; Zhu, Y.-C.; Zhao, W.-W.; Yu, X.-D.; Xu, J.-J.; Chen, H.-Y. 3D semiconducting polymer/graphene networks: toward sensitive photocathodic enzymatic bioanalysis. *Anal. Chem.* **2018**, *90* (16), 9687–9690.
- (28) Ghosh, T. K.; Gope, S.; Mondal, D.; Bhowmik, B.; Mollick, M. M. R.; Maity, D.; Roy, I.; Sarkar, G.; Sadhukhan, S.; Rana, D.; et al. Assessment of morphology and property of graphene oxide-hydroxypropylmethylcellulose nanocomposite films. *Int. J. Biol. Macromol.* **2014**, *66*, 338–345.
- (29) He, Y.; Del Valle, A.; Qian, Y.; Huang, Y.-F. Near infrared light-mediated enhancement of reactive oxygen species generation through electron transfer from graphene oxide to iron hydroxide/oxide. *Nanoscale* **2017**, *9* (4), 1559–1566.
- (30) Mansoori, S.; Davarnejad, R.; Ozumchelouei, E. J.; Ismail, A. F. Activated biochar supported iron-copper oxide bimetallic catalyst for degradation of ciprofloxacin via photo-assisted electro-Fenton process: a mild pH condition. *J. Water Process. Eng.* **2021**, *39*, No. 101888.
- (31) Wei, J.; Zang, Z.; Zhang, Y.; Wang, M.; Du, J.; Tang, X. Enhanced performance of light-controlled conductive switching in hybrid cuprous oxide/reduced graphene oxide (Cu₂O/rGO) nanocomposites. *Opt. Lett.* **2017**, *42* (5), 911–914.
- (32) Jia, X.; Lian, D.; Shi, B.; Dai, R.; Li, C.; Wu, X. Facile synthesis of α -Fe₂O₃@graphene oxide nanocomposites for enhanced gas-sensing performance to ethanol. *J. Mater. Sci.: Mater.* **2017**, *28* (16), 12070–12079.
- (33) Liu, Z.; Lv, B.; Wu, D.; Sun, Y.; Xu, Y. Preparation and Properties of Octadecahedral α -Fe₂O₃ Nanoparticles Enclosed by {104} and {112} Facets. *Eur. J. Inorg. Chem.* **2012**, *2012* (25), 4076–4081.
- (34) Hua, J.; Gengsheng, J. Hydrothermal synthesis and characterization of monodisperse α -Fe₂O₃ nanoparticles. *Mater. Lett.* **2009**, *63* (30), 2725–2727.
- (35) Agouriane, E.; Rabi, B.; Essoumhi, A.; Razouk, A.; Sahlaoui, M.; Costa, B.; Sajieddine, M. Structural and magnetic properties of CuFe₂O₄ ferrite nanoparticles synthesized by co-precipitation. *J. Mater. Environ. Sci.* **2016**, *7* (11), 4116–4120.
- (36) Dong, Y.-l.; Zhang, X.-f.; Cheng, X.-l.; Xu, Y.-m.; Gao, S.; Zhao, H.; Huo, L.-h. Highly selective NO₂ sensor at room temperature based on nanocomposites of hierarchical nanosphere-like α -Fe₂O₃ and reduced graphene oxide. *RSC Adv.* **2014**, *4* (101), 57493–57500.
- (37) Vasseghian, Y.; Sezgin, D.; Nguyen, D. C.; Hoang, H. Y.; Yilmaz, M. S. A hybrid nanocomposite based on CuFe layered double hydroxide coated graphene oxide for photocatalytic degradation of trimethoprim. *Chemosphere* **2023**, *322*, No. 138243.
- (38) Garcia Rojas, L. M.; Huerta-Aguilar, C. A.; Navarrete, E.; Llobet, E.; Thangarasu, P. Enhancement of the CO₂ Sensing/Capture through High Cationic Charge in M-ZrO₂ (Li⁺, Mg²⁺, or Co³⁺): Experimental and Theoretical Studies. *ACS Appl. Mater. Interfaces.* **2023**, *15* (21), 25952–25965.
- (39) Zhao, X.; Tan, Y.; Wu, F.; Niu, H.; Tang, Z.; Cai, Y.; Giesy, J. P. Cu/Cu₂O/CuO loaded on the carbon layer derived from novel precursors with amazing catalytic performance. *Sci. Total Environ.* **2016**, *571*, 380–387.
- (40) Ye, J.; Wang, Y.; Xu, Q.; Wu, H.; Tong, J.; Shi, J. Removal of hexavalent chromium from wastewater by Cu/Fe bimetallic nanoparticles. *Sci. Rep.* **2021**, *11* (1), 10848.
- (41) Faheem, M.; Jiang, X.; Wang, L.; Shen, J. Synthesis of Cu₂O–CuFe₂O₄ microparticles from Fenton sludge and its application in the Fenton process: the key role of Cu₂O in the catalytic degradation of phenol. *RSC Adv.* **2018**, *8* (11), 5740–5748.
- (42) García-Gutiérrez, Y. S.; Huerta-Aguilar, C. A.; Thangarasu, P.; Vázquez-Ramos, J. M. Ciprofloxacin as chemosensor for simultaneous recognition of Al³⁺ and Cu²⁺ by Logic Gates supported fluorescence: Application to bio-imaging for living cells. *Sens. Actuators B Chem.* **2017**, *248*, 447–459.
- (43) He, B.; Song, L.; Zhao, Z.; Liu, W.; Zhou, Y.; Shang, J.; Cheng, X. J. E. J. CuFe₂O₄/CuO magnetic nano-composite activates PMS to remove ciprofloxacin: Ecotoxicity and DFT calculation. *Chem. Eng. J.* **2022**, *446*, No. 137183.
- (44) Santos, A. M.; Wong, A.; Almeida, A. A.; Fatibello-Filho, O. Simultaneous determination of paracetamol and ciprofloxacin in biological fluid samples using a glassy carbon electrode modified with graphene oxide and nickel oxide nanoparticles. *Talanta* **2017**, *174*, 610–618.

- (45) Zhang, X.; Wei, Y.; Ding, Y. Electrochemical oxidation and voltammetric determination of ciprofloxacin employing poly (alizarin red)/graphene composite film in the presence of ascorbic acid, uric acid and dopamine. *Anal. Chim. Acta* **2014**, *835*, 29–36.
- (46) Tecuapa-Flores, E. D.; Hernández, J. G.; Roquero-Tejeda, P.; Arenas-Alatorre, J. A.; Thangarasu, P. Rapid electrochemical recognition of trimethoprim in human urine samples using new modified electrodes (CPE/Ag/Au NPs) analysing tunable electrode properties: experimental and theoretical studies. *Analyst* **2021**, *146* (24), 7653–7669.
- (47) Li, J.; Huang, X.; Ma, J.; Wei, S.; Zhang, H. A novel electrochemical sensor based on molecularly imprinted polymer with binary functional monomers at Fe-doped porous carbon decorated Au electrode for the sensitive detection of lomefloxacin. *Ionics* **2020**, *26* (8), 4183–4192.
- (48) Li, L.; Fu, Y.; Manthiram, A. Imidazole-buffered acidic catholytes for hybrid Li–air batteries with high practical energy density. *Electrochem. commun.* **2014**, *47*, 67–70.
- (49) Zhao, J.; Huang, P.; Jin, W. Electrochemical sensor based on TiO₂/polyvinyl alcohol nanocomposite for detection of ciprofloxacin in rainwater. *Int. J. Electrochem. Sci.* **2021**, *16* (10), 211018.
- (50) Cai, Y.; Zhang, Y.; Su, S.; Li, S.; Ni, Y. Electrochemical studies oxidation of ciprofloxacin at nano-SnO₂/PVS modified electrode and its interaction with calf thymus DNA. *Front. Biosci.* **2007**, *12*, 1946–1955.
- (51) Gissawong, N.; Srijaranai, S.; Boonchiangma, S.; Uppachai, P.; Seehamart, K.; Jantrasee, S.; Moore, E.; Mukdasai, S. An electrochemical sensor for voltammetric detection of ciprofloxacin using a glassy carbon electrode modified with activated carbon, gold nanoparticles and supramolecular solvent. *Mikrochim. Acta* **2021**, *188* (6), 208.
- (52) Miseki, Y.; Sayama, K. Photocatalytic water splitting employing a [Fe(CN)₆]^{3-/4-} redox mediator under visible light. *Catal. Sci. Technol.* **2019**, *9* (8), 2019.
- (53) Al-Namshah. Impact of CuO incorporation on the photocatalytic enhancement of the mesostructured Fe₂O₃ nanocomposite. *Appl. Nanosci.* **2021**, *11*, 467–476.
- (54) Yuan, Y.; Zhang, F.; Wang, H.; Gao, L.; Wang, Z. A sensor based on Au nanoparticles/carbon nitride/graphene composites for the detection of chloramphenicol and ciprofloxacin. *ECS J. Solid State Sci. Technol.* **2018**, *7* (12), M201.
- (55) Surya, S. G.; Khatoon, S.; Lahcen, A. A.; Nguyen, A. T.; Dzantiev, B. B.; Tarannum, N.; Salama, K. N. A chitosan gold nanoparticles molecularly imprinted polymer based ciprofloxacin sensor. *RSC Adv.* **2020**, *10* (22), 12823–12832.
- (56) Yahyapour, M.; Ranjbar, M.; Mohadesi, A. Determination of ciprofloxacin drug with molecularly imprinted polymer/co-metal organic framework nanofiber on modified glassy carbon electrode (GCE). *J. Mater. Sci. Mater. Electron* **2021**, *32*, 3180–3190.
- (57) Ensafi, A. A.; Allafchian, A. R.; Mohammadzadeh, R. Characterization of MgFe₂O₄ nanoparticles as a novel electrochemical sensor: application for the voltammetric determination of ciprofloxacin. *Anal. Sci.* **2012**, *28* (7), 705–710.
- (58) Fang, X.; Chen, X.; Liu, Y.; Li, Q.; Zeng, Z.; Maiyalagan, T.; Mao, S. Nanocomposites of Zr (IV)-based metal–organic frameworks and reduced graphene oxide for electrochemically sensing ciprofloxacin in water. *ACS Appl. Nano Mater.* **2019**, *2* (4), 2367–2376.
- (59) Vedhavathi, H. S.; Sanjay, B. P.; Basavaraju, M.; Madhukar, B. S.; Swamy, N. K. Development of ciprofloxacin sensor using iron-doped graphitic carbon nitride as transducer matrix: Analysis of ciprofloxacin in blood samples. *J. Electrochem. Sci. Eng.* **2022**, *12* (1), 59–70.
- (60) Pienutsa, N.; Roongruangsree, P.; Seedokbuab, V.; Yannawibut, K.; Phatoomvijitwong, C.; Srinives, S. SnO₂-graphene composite gas sensor for a room temperature detection of ethanol. *Nanotechnology* **2021**, *32* (11), 115502.
- (61) Yang, N.; Liu, Y.; Wen, H.; Tang, Z.; Zhao, H.; Li, Y.; Wang, D. Photocatalytic properties of graphdiyne and graphene modified TiO₂: from theory to experiment. *ACS Nano* **2013**, *7* (2), 1504–1512.